ARCHIVE OF MECHANICAL ENGINEERING

DOI: 10.24425/ame.2026.12678 Early Access; pp. 1–39

Mohamed LATRACHE [1]

Verifying finite-element buckling of columns and plates: an educational study with mode transitions

Received 13 August 2026, **Revised** 5 November 2026, **Accepted** 10 November 2026, **Published online** 19 November 2026

Keywords: elastic buckling, Euler column, rectangular plate, finite element method, mode transition, transverse-shear deformation, engineering education, verification and validation

This educational case study shows, step by step, how analytical solutions verify finite-element buckling eigenvalue models for a pinned-pinned Euler-Bernoulli column and a simply supported rectangular plate under uniaxial compression. For the column, a 40-element cubic-Hermite beam model yields a first critical load of 27.634894 kN, compared with 27.634892 kN analytically (5.28×10^{-6}% error), allowing students to check the stiffness matrices, sign conventions, and mesh convergence. For the plate, the governing mode is identified by modal minimization and verified with an in-house Q4 flat-shell model (60×40 mesh: 329.645 kN/m, +0.040% versus Navier). An ANSYS SHELL181 refinement from 6×4 to 48×32 elements reduces the first-mode error from 17.42% to 0.547%, and the remaining error is limited mainly by the equal nodal partition of the edge load. The classical transition relation $a/b = \sqrt{m(m+1)}$ is used as the reference: both shell models locate the first two mode transitions, which converge to the Mindlin values rather than the thin-plate ones (1.4138 for $b/t = 100$ and 1.4030 for $b/t = 20$, instead of $\sqrt{2}$). Learning objectives, documented conventions, and exercises are provided, and the data are openly deposited.

1. Introduction

Structural stability matters in the design of slender components across mechanical, aerospace, marine, and civil engineering: columns, machine frames, stiffened panels, aircraft skins, and other thin-walled or plate-like parts. Under compression,

✉ Mohamed LATRACHE, email: mohamed.latrache@univ-msila.dz

[1]Department of Mechanical Engineering, Faculty of Technology, University of M'sila, M'sila, Algeria.

© 2026. The Author(s). This is an open-access article distributed under the terms of the Creative Commons Attribution (CC-BY 4.0, https://creativecommons.org/licenses/by/4.0/), which permits use, distribution, and reproduction in any medium, provided that the author and source are cited.

they can lose stability suddenly, even while the material is still elastic, so a strength criterion alone does not guarantee safety [1–4].

For an ideal slender column, the onset of buckling is described by classical Euler theory, in which the critical load depends on the flexural rigidity, the effective length, and the end restraints. The Euler solution is well established, yet it remains an essential benchmark for checking numerical discretizations and finite-element implementations. A reliable model has to reproduce not only the first critical load but also the higher eigenvalues and their deformation patterns [1, 2, 5–7].

Thin rectangular plates behave in a more complicated way. Their critical load depends on the two-dimensional geometry, the bending rigidity, the boundary conditions, the loading direction, and the number of half-waves formed in each direction. The governing mode is not necessarily the one with a single longitudinal half-wave; it comes from minimizing the critical-load expression over the admissible modal integers [3, 8–10].

Linear finite-element eigenvalue analysis is widely used to estimate ideal elastic critical loads, but its accuracy depends on the element formulation, mesh density, boundary-condition implementation, reference load, and geometric stiffness matrix. A systematic comparison with analytical solutions, together with a quantitative convergence study, is therefore needed before a model is extended to more complex structures.

Elastic buckling is also one of the most instructive topics in courses on structural stability, mechanics of materials, and the finite element method, because every quantity a student computes numerically has a closed-form counterpart. The Euler formula, the plate buckling coefficient, and the finite-element eigenvalue problem are usually met in separate courses, however, and a single worked case that compares all three, with documented conventions, quantified errors, and reproducible files, is seldom available. This paper is an educational case study that fills that gap with a complete, verifiable, and reusable example built on classical results.

Recent computational stability research uses finite elements, meshless and differential-quadrature formulations, enriched approximations, nonlinear path-following, and experiment-informed validation. Patil and Kadoli reviewed differential-quadrature formulations for beam and plate problems, with emphasis on discretization and convergence [11], and Patel et al. used modified Fourier and differential-quadrature solutions for plate response under varied boundary conditions, which shows the value of cross-method verification [12]. For simply supported rectangular plates under uniaxial thrust, the modal buckling coefficient and the selection of the longitudinal half-wave number are classical results [3, 8–10]. Numerical spectral studies of plate buckling show that multiple eigenvalues need careful discretization, and earlier work has treated buckled states at double eigenvalues explicitly [13, 14]. The present study uses these known crossings as a more demanding verification target: rather than reproducing a critical load at a single geometry, it quantifies how mesh refinement in an independently assembled Q4 eigenproblem localizes the first two branch crossings. Exact relationships between Kirchhoff and Mindlin buckling

loads [15–17] and exact Mindlin solutions for rectangular plates [18] are available, and the latter show that the half-wave number of the critical mode depends on the thickness ratio. The shear-shifted transition aspect ratios of the simply supported plate under uniaxial compression are mapped here using Reissner-Mindlin theory, and their effect is separated from finite-element discretization error [19, 20].

The learning objectives are to show how to: (i) verify the Euler column spectrum with an independently assembled finite-element eigenvalue model and quantify its convergence and length sensitivity; (ii) document the reference-load, sign, assembly, constraint, and eigenvalue-sorting conventions that most often cause errors in student codes; (iii) distinguish analytical stability indicators from matrix-based finite-element energy checks, and read the imperfection relation strictly as a pre-critical analytical illustration; (iv) formulate the plate problem in dimensionless form and carry out the complete modal minimization; (v) verify the plate with an independent Q4 flat-shell eigenvalue model and with an ANSYS Mechanical APDL 2021 R1 SHELL181 mesh-refinement study, including mode-shape comparison and the effect of load introduction; (vi) locate numerically the first two double-eigenvalue mode-transition points and interpret the mesh-dependent localization error; (vii) examine thickness, aspect-ratio, and Poisson-ratio sensitivities within classical thin-plate theory; and (viii) separate discretization error from model-form error through the transverse-shear shift of the transition points as a function of b/t.

The paper follows a teaching sequence: Section 2 states the theory and the finite-element formulation, Section 3 describes the computational models, and Section 4 presents the results, each tied to the verification question it answers, followed by the Discussion, the limitations, and the Conclusions. The classical relation $a/b = \sqrt{m(m+1)}$ is used as the reference condition for the mode transitions. The MATLAB/MAT/CSV/PNG outputs and the independent verification calculations (Q4 flat shell, ANSYS SHELL181, transition localization, transverse shear, audits) are deposited in separate supplementary folders so that instructors can reuse each part on its own. The paper is meant for instructors and students of structural stability and computational mechanics, and for practitioners who want to check their own eigenvalue-buckling workflows.

Suggested use in teaching. Sections 2.1–2.5, 4.1–4.5, and 4.13 can support a lecture or laboratory on the column (derive Eq. (4), assemble the matrices of Eqs. (12)–(13), and reproduce the convergence order of Eq. (17)), and Sections 2.6–2.8 and 4.6–4.12 a session on plate modal minimization and shell-element verification. Possible exercises: (a) reproduce the column eigenvalues with 2, 4, and 8 elements and estimate the observed order from Eq. (17); (b) find by direct modal minimization the governing (m, n) pair for $a/b = 1.5$ and confirm that two longitudinal half-waves govern; (c) use the Q4 element or any shell element to find the aspect ratio at which the governing m changes from 1 to 2 and compare it with $\sqrt{2}$; (d) repeat (c) with transverse shear for $b/t = 20$ and explain why the transition

lies below $\sqrt{2}$; and (e) compare an equal nodal partition of the edge load with a consistent load and discuss the difference in convergence rate.

2. Theoretical formulation

2.1. Euler-Bernoulli column under axial compression

Consider a straight, prismatic column of length L, Young's modulus E, and second moment of area I, subjected to a compressive axial load P. Under the assumptions of Euler-Bernoulli beam theory, the transverse displacement $w(x)$ satisfies:

$$EI\frac{d^4w}{dx^4} + P\frac{d^2w}{dx^2} = 0. \tag{1}$$

For a column simply supported at both ends, the kinematic boundary conditions are:

$$w(0) = w(L) = 0. \tag{2}$$

An admissible buckling mode is:

$$w_n(x) = A_n \sin\left(\frac{n\pi x}{L}\right), \qquad n = 1, 2, 3, \ldots \tag{3}$$

where n denotes the buckling-mode number. Substitution into the governing differential equation gives the classical Euler eigenvalues:

$$P_{cr,n} = \frac{n^2\pi^2 EI}{L^2}. \tag{4}$$

The first critical load is therefore

$$P_{cr,1} = \frac{\pi^2 EI}{L^2}, \tag{5}$$

and the higher critical loads satisfy

$$P_{cr,n} = n^2 P_{cr,1}. \tag{6}$$

For an ideal simply supported column, the second, third, and fourth buckling loads are therefore four, nine, and sixteen times the first critical load.

2.2. Energy-based stability criterion

The total potential energy of a compressed Euler-Bernoulli column may be written in quadratic form as:

$$\Pi[w] = \frac{1}{2}\int_0^L EI\left(\frac{d^2w}{dx^2}\right)^2 dx - \frac{P}{2}\int_0^L \left(\frac{dw}{dx}\right)^2 dx. \tag{7}$$

For the first sinusoidal mode,

$$w(x) = A\sin\left(\frac{\pi x}{L}\right), \tag{8}$$

the second variation of the total potential energy is proportional to

$$\delta^2\Pi \propto P_{cr,1} - P. \tag{9}$$

A normalized stability indicator can be defined as:

$$\mathcal{S} = 1 - \frac{P}{P_{cr,1}}. \tag{10}$$

The equilibrium classification follows directly. The straight state is stable for $\mathcal{S} > 0$, critical or neutrally stable for $\mathcal{S} = 0$, and unstable for $\mathcal{S} < 0$. At the critical load, the quadratic stiffness associated with a lateral perturbation vanishes, thereby allowing a nontrivial equilibrium configuration to bifurcate from the straight state [2, 4, 21, 22].

2.3. Finite element formulation of the column

The column is discretized using two-node Euler-Bernoulli beam elements. Each node has two degrees of freedom: transverse displacement and cross-sectional rotation. The element displacement vector is:

$$\mathbf{q}_e = \begin{bmatrix} w_1 & \theta_1 & w_2 & \theta_2 \end{bmatrix}^T. \tag{11}$$

For an element of length L_e, the elastic bending stiffness matrix is:

$$\mathbf{K}_e = \frac{EI}{L_e^3}\begin{bmatrix} 12 & 6L_e & -12 & 6L_e \\ 6L_e & 4L_e^2 & -6L_e & 2L_e^2 \\ -12 & -6L_e & 12 & -6L_e \\ 6L_e & 2L_e^2 & -6L_e & 4L_e^2 \end{bmatrix}. \tag{12}$$

The geometric stiffness matrix associated with a unit compressive reference load is:

$$\mathbf{K}_{G,e} = \frac{1}{30L_e}\begin{bmatrix} 36 & 3L_e & -36 & 3L_e \\ 3L_e & 4L_e^2 & -3L_e & -L_e^2 \\ -36 & -3L_e & 36 & -3L_e \\ 3L_e & -L_e^2 & -3L_e & 4L_e^2 \end{bmatrix}. \tag{13}$$

After assembling the global elastic and geometric stiffness matrices and imposing the simply supported boundary conditions, the buckling problem takes the generalized eigenvalue form:

$$\mathbf{K}\varphi = \lambda \mathbf{K}_G \varphi, \tag{14}$$

where λ is the critical load factor and φ the corresponding discrete buckling mode. The reference state is a uniform compressive axial force $P_0 = 1$ N in every beam element, with compression taken as positive in the geometric-stiffness contribution, so the assembled eigenproblem is $(\mathbf{K} - \lambda \mathbf{K}_G)\varphi = 0$ and λ has units of force. The unit state is not applied as separate nodal loads; it stands for one uniform axial-force field from which each element geometric matrix is assembled. After global assembly, the constrained transverse-displacement degrees of freedom at the two pinned ends are eliminated from both $\mathbf{K}$ and $\mathbf{K}_G$, and the finite positive eigenvalues are retained and sorted in ascending order. With $P_0 = 1$ N, the physical critical loads are numerically equal to the positive eigenvalues λ:

$$P_{cr}^{FE} = \lambda. \tag{15}$$

2.4. Mesh convergence error

The relative error between the finite-element critical load and the analytical Euler result is evaluated using:

$$e_h = \left| \frac{P_{cr}^{FE} - P_{cr}^{analytical}}{P_{cr}^{analytical}} \right| \times 100\%. \tag{16}$$

When two successive meshes are related by a constant refinement ratio, the observed convergence order is estimated as:

$$p_{obs} = \frac{\ln\left(e_{h_1}/e_{h_2}\right)}{\ln\left(h_1/h_2\right)}. \tag{17}$$

For uniform refinement in which the number of elements is doubled, $h_1/h_2 = 2$.

2.5. Initial imperfection amplification

Real columns are not perfectly straight and may contain initial geometric imperfections. For a column with an initial sinusoidal imperfection amplitude w_0, the linear elastic amplification relation is:

$$w_{\max} = \frac{w_0}{1 - P/P_{cr}}. \tag{18}$$

This expression predicts rapid growth of the lateral displacement as the load approaches the Euler critical load from below. It holds only in the linear pre-buckling range and gives no complete post-buckling description, which would need geometric nonlinearity.

2.6. Buckling of a simply supported rectangular plate

Consider a thin isotropic rectangular plate of length a, width b, thickness t, Young's modulus E, and Poisson's ratio ν. The plate is simply supported along its four edges and subjected to a uniform in-plane compressive membrane load N_x in the x-direction. The plate flexural rigidity is:

$$D = \frac{Et^3}{12\left(1 - \nu^2\right)}. \tag{19}$$

According to classical thin-plate theory, the buckling equation is:

$$D\nabla^4 w + N_x \frac{\partial^2 w}{\partial x^2} = 0. \tag{20}$$

A modal displacement satisfying the simply supported boundary conditions is assumed as:

$$w_{mn}(x, y) = W_{mn} \sin\left(\frac{m\pi x}{a}\right) \sin\left(\frac{n\pi y}{b}\right), \tag{21}$$

where m and n are positive integers representing the numbers of half-waves in the x- and y-directions. Substitution into the governing equation yields

$$N_{x,cr}^{(m,n)} = \frac{\pi^2 D}{a^2} \frac{\left[m^2 + n^2(a/b)^2\right]^2}{m^2}. \tag{22}$$

The governing plate buckling load is obtained through the discrete minimization:

$$N_{x,cr} = \min_{m,n} N_{x,cr}^{(m,n)}. \tag{23}$$

The corresponding average critical compressive stress is:

$$\sigma_{cr} = \frac{N_{x,cr}}{t}, \tag{24}$$

and the equivalent total critical load acting along a loaded edge of width b is

$$P_{cr,\text{total}} = N_{x,cr}\, b. \tag{25}$$

2.7. Classical mode-transition boundaries and Poisson-ratio sensitivity

For the simply supported isotropic plate compressed in the x-direction, the classical modal expression increases strictly with the transverse modal integer n for fixed m and $a/b > 0$, so $n = 1$ minimizes the critical load. This property provides a precise benchmark for the independent numerical model [3, 8–10].

Let $r = a/b$. With $n = 1$, the plate eigenvalue can be written in terms of the dimensionless coefficient $k_m(r)$ as:

$$N_{x,cr} = \frac{\pi^2 D}{b^2} k_m, k_m = \left(\frac{m}{r} + \frac{r}{m}\right)^2. \tag{26}$$

Two adjacent longitudinal modes exchange order when $k_m(r) = k_{m+1}(r)$. All quantities are positive, so taking the positive square root and simplifying gives:

$$\frac{m}{r} + \frac{r}{m} = \frac{m+1}{r} + \frac{r}{m+1} \tag{27}$$

which reduces exactly to:

$$r^2 = m(m+1), \quad r = \sqrt{m(m+1)}. \tag{28}$$

Accordingly, longitudinal mode m governs within the exact interval:

$$\sqrt{m(m-1)} < r < \sqrt{m(m+1)}. \tag{29}$$

Adjacent branches meet at $r = \sqrt{m(m+1)}$. At such a transition modes m and $m+1$ share the same eigenvalue and coexist, so the governing mode is not unique exactly at the boundary. Away from a transition, mode m governs for $\sqrt{m(m-1)} < r < \sqrt{m(m+1)}$ (the lower bound is zero for $m = 1$). The first two transition points are $\sqrt{2} \approx 1.41421356$ and $\sqrt{6} \approx 2.44948974$; they serve below as reference values for checking the discrete MATLAB sweep and the independent flat-shell calculation. A related dependence of the critical number of half-waves on the aspect ratio, together with mode jumping in the post-buckling range, is discussed for unsymmetric laminated plates [23].

The same closed-form solution also shows the influence of Poisson's ratio. Since $D = Et^3/[12(1-\nu^2)]$ and the modal factor does not depend on ν, the critical membrane load satisfies:

$$N_{x,cr}(\nu) = \frac{N_{x,cr}(0)}{1-\nu^2}, \tag{30}$$

and its logarithmic sensitivity is:

$$S_\nu = \frac{\nu}{N_{x,cr}}\frac{dN_{x,cr}}{d\nu} = \frac{2\nu^2}{1-\nu^2}. \tag{31}$$

2.8. Transverse shear (Mindlin) reference for the mode transition points

The Q4 and SHELL181 models used in Sections 4.7 and 4.9.1 are first-order shear-deformation (Reissner-Mindlin) formulations [19, 20, 24], whereas the benchmark of Sections 2.6 and 2.7 is a Kirchhoff plate. For the hard simply supported plate ($w = 0$ on all edges, $\psi_y = 0$ on $x = 0$ and $x = a$, $\psi_x = 0$ on $y = 0$ and $y = b$), the Mindlin equilibrium equations under a uniform compressive resultant N_x are satisfied by $w = W\sin(\alpha x)\sin(\beta y)$, $\psi_x = -\alpha\varphi\cos(\alpha x)\sin(\beta y)$, and $\psi_y = -\beta\varphi\sin(\alpha x)\cos(\beta y)$, with $\alpha = m\pi/a$, $\beta = n\pi/b$, and $\lambda^2 = \alpha^2 + \beta^2$. Eliminating $\varphi = \kappa G t W/(D\lambda^2 + \kappa G t)$ from the rotation equations gives:

$$N^M_{x,cr}(m,n) = \frac{N^K_{x,cr}(m,n)}{1 + \frac{D\lambda^2}{\kappa G t}}, \tag{31a}$$

where $N^K_{x,cr}(m,n) = D\lambda^4/\alpha^2$ on the right-hand side is the Kirchhoff value of Section 2.6, κ is the shear-correction factor ($\kappa = 5/6$ throughout), and $G = E/[2(1+\nu)]$. Equation (31a) reduces to the Kirchhoff result as $\kappa G t \to \infty$. Exact relationships between Kirchhoff and Mindlin buckling loads are known for simply supported polygonal plates under isotropic in-plane load [15–17], and exact Mindlin buckling solutions for rectangular plates with several boundary conditions are available [18]; the governing equations of initially stressed Mindlin plates, on which these analyses rest, appear in [25]. Equation (31a) is the corresponding Navier-type expression for uniaxial compression; the λ^2-dependence of the correction is what shifts the transitions.

The correction factor depends on λ^2 and therefore differs between neighboring longitudinal branches. Equality of the branches m and $m+1$ ($n = 1$) no longer occurs at $a/b = \sqrt{m(m+1)}$; the shear-shifted transition $r^*_m(b/t)$ is the root of the equation obtained by equating the Mindlin loads of Eq. (31a) for the branches $(m, 1)$ and $(m+1, 1)$. For small shear flexibility, the shift is of order $\varepsilon = \pi^2 t^2/[6\kappa(1-\nu)b^2]$, that is, proportional to $(t/b)^2$, and negative: the transitions move toward smaller aspect ratios. For the benchmark plate ($b/t = 100$) the Mindlin load of the (2,1) mode at $a/b = 1.5$ is 329.256 kN/m, 0.078% below the Kirchhoff value of 329.514 kN/m, and the first two transitions are $r^*_1 = 1.413765$ and $r^*_2 = 2.448770$ instead of $\sqrt{2}$ and $\sqrt{6}$. Equation (31a) holds for hard support; with only $w = 0$ imposed (soft support) the loads are lower (Section 4.9.3).

3. Numerical procedure

3.1. Column model

A simply supported steel column with Young's modulus $E = 210$ GPa and length $L = 1.0$ m was considered. The column has a square cross-section of side 20 mm, giving:

$$I = \frac{(0.02)^4}{12} = 1.33333 \times 10^{-8} \text{ m}^4. \tag{32}$$

The analytical Euler loads were computed for the first four modes. The MATLAB source sets `nElem= 40` for the production run; Table 1 and Fig. 1 use this 40-element mesh, which reproduces all the finite-element values reported here. The same source defines the convergence sequence as 2, 4, 8, 16, 32, 64, and 100 uniform elements. Observed orders are evaluated only for the doubling sequence up to 64 elements; the 100-element result serves as an extra precision check and stays out of the doubling-rate estimate.

3.2. Plate model

The isotropic rectangular plate was defined by $a = 0.60$ m, $b = 0.40$ m, $t = 0.004$ m, $E = 210$ GPa, and $\nu = 0.30$. Its bending rigidity is:

$$D = 1230.769 \text{ N·m}. \tag{33}$$

The analytical benchmark for the plate is a modal search over positive integers m and n. Two separate finite-element routes provide independent numerical checks. The first is the transverse buckling block of a four-node Q4 flat-shell element with Reissner-Mindlin variables (w, β_x, β_y), 2×2 Gauss integration of bending, and MITC-type tying of the transverse shear strains [24] on aligned rectangular meshes. To match the Navier benchmark, hard simple support is imposed: $w = 0$ on all four edges, $\beta_y = 0$ on $x = 0, a$, and $\beta_x = 0$ on $y = 0, b$. A uniform reference membrane resultant $N_{x,0} = 1$ N/m defines the geometric stiffness, and $(\mathbf{K} - \lambda \mathbf{K}_G)\varphi = 0$ is solved, keeping the positive finite eigenvalues in ascending order. Meshes from 6×4 to 60×40 elements are reported. The second route is ANSYS Mechanical APDL 2021 R1 with SHELL181. A structured refinement series with 6×4, 12×8, 24×16, and 48×32 meshes uses the same material and geometry, UZ = 0 edge supports, minimal in-plane rigid-body restraints, static prestress, and Block Lanczos extraction. The total 1 N compressive reference edge load is divided equally among the selected $x = a$ edge nodes, as in the APDL script. A separate 1080-element production-resolution run supplies raw solver output and first-four mode data. The project APDL deck and the convergence deck are provided separately.

For comparison across scales, the column eigenvalues can be written in the dimensionless form $\bar{P} = P_{cr}L^2/(EI) = n^2\pi^2$. For the plate, the dimensionless buckling coefficient is $k = N_{x,cr}b^2/(\pi^2 D) = (m/r + r/m)^2$ for $n = 1$, with $r = a/b$. These forms separate the modal and aspect-ratio dependence from the dimensional stiffness and length scales, and they serve as reproducibility checks in the supplementary data.

3.3. Parametric investigations

The computational study covers the first four column eigenvalues, the beam mesh convergence, analytical stability and imperfection sweeps, plate modal minimization, thickness and aspect-ratio sweeps, and mode-transition data. It also includes matrix-based FE energy checks, an archive-consistency audit, the Q4 flat-shell convergence and mode-shape calculation, the structured ANSYS SHELL181 refinement series, the production-resolution ANSYS run, and a Q4 transition-localization test around the first two double-eigenvalue crossings. In the aspect-ratio sweep, $b = 0.40$ m and $t = 4$ mm are held fixed while $a = rb$ varies, with E and ν unchanged; the transition-localization test uses the same update rule, so the numerical crossing locations can be compared directly with $\sqrt{2}$ and $\sqrt{6}$.

4. Results

The results are grouped by evidence type: closed-form analytical benchmarks, the MATLAB source and its outputs, analytical parameter sweeps, in-house Q4 finite-element verification, and ANSYS SHELL181 verification. The Q4 and ANSYS refinement studies are reported together in Section 4.7, and the 1080-element ANSYS production run is kept as an extra cross-check. This separation shows which results are analytical, which come from the MATLAB study, and which come from independent verification models.

4.1. Column eigenvalues and buckling mode shapes

Table 1 compares the analytical Euler eigenvalues with those of the independently assembled beam finite-element model. The first four finite-element loads follow the theoretical n^2 scaling, and the relative error stays below 0.0014% even for the fourth mode.

The first critical load is 27.634892 kN analytically and 27.634894 kN numerically. Fig. 1 shows the first three normalized MATLAB mode shapes with their critical loads; the number of half-waves grows with the mode number, as the simply supported boundary conditions require.

Table 1. Complete analytical-finite-element comparison for the first four column buckling modes (40-element production mesh)

Mode n	Analytical P_{cr} (kN)	FE P_{cr} (kN)	Relative error (%)
1	27.634892	27.634894	5.283820e-06
2	110.539569	110.539663	8.444739e-05
3	248.714031	248.715092	4.268276e-04
4	442.158277	442.164228	1.345961e-03

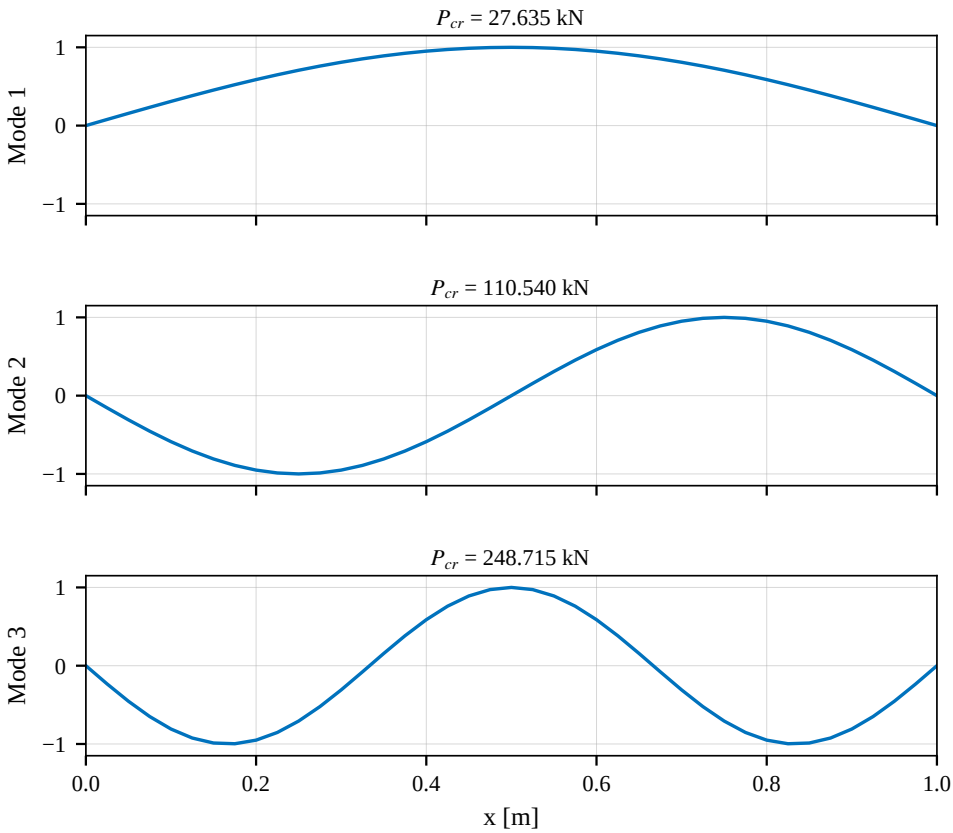


Fig. 1. MATLAB-generated first three normalized column buckling modes and associated finite-element critical loads

4.2. Mesh convergence assessment

The beam convergence sequence (Table 2, Fig. 2) uses 2, 4, 8, 16, 32, 64, and 100 Euler-Bernoulli elements. Over the successive doublings up to 64 elements, the observed orders are 3.8766, 3.9663, 3.9913, 3.9979, and 3.9767, which confirms the fourth-order eigenvalue convergence expected from cubic interpolation in the asymptotic range. At the smallest errors, eigensolver tolerance and double-precision round-off contaminate the rate estimates, so no order is inferred from the 64-to-100 refinement. The 40-element production mesh of Table 1 and Fig. 1 is not part of the doubling sequence either, but its first-mode error of $5.28\times10^{-6}\%$ matches, to three significant digits, the 32-element error of Table 2 scaled by $(32/40)^4$, which gives $5.28\times10^{-6}\%$, as fourth-order convergence predicts. Table 1 is therefore consistent with Table 2.

Table 2. Complete mesh-convergence sequence for the first column critical load. The observed order p is reported only for successive mesh doublings

Elements	FE $P_{cr,1}$ (kN)	Relative error (%)	Observed p
2	27.842771030	7.522327e-01	—
4	27.649045272	5.121405e-02	3.8766
8	27.635797810	3.276609e-03	3.9663
16	27.634949257	2.060211e-04	3.9913
32	27.634895887	1.289510e-05	3.9979
64	27.634892549	8.190781e-07	3.9767
100	27.634892365	1.533601e-07	n/a

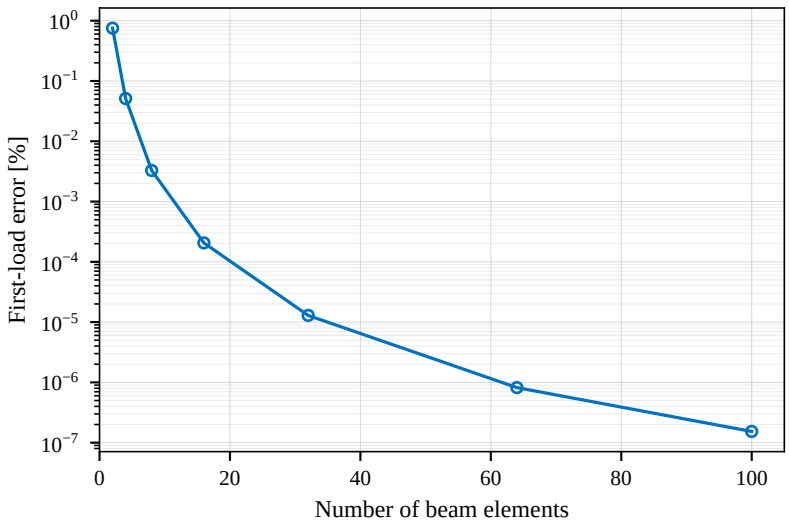


Fig. 2. Original MATLAB mesh-convergence plot for the first column buckling eigenvalue

4.3. Sensitivity of the column critical load to length

The MATLAB sweep (Table 3, Fig. 3) covers column lengths from 0.40 to 2.00 m, over which the critical load falls from 172.718 kN to 6.909 kN. The curve follows $P_{cr} \propto L^{-2}$ exactly for the prismatic pinned-pinned column: doubling the length from 0.50 to 1.00 m cuts the critical load from 110.540 to 27.635 kN, a factor of four.

Table 3. Representative values from the complete 81-point column-length sensitivity sweep

Column length L (m)	Critical load P_{cr} (kN)
0.40	172.718077
0.50	110.539569
0.60	76.763590
0.80	43.179519
1.00	27.634892
1.20	19.190897
1.40	14.099435
1.60	10.794880
1.80	8.529288
2.00	6.908723

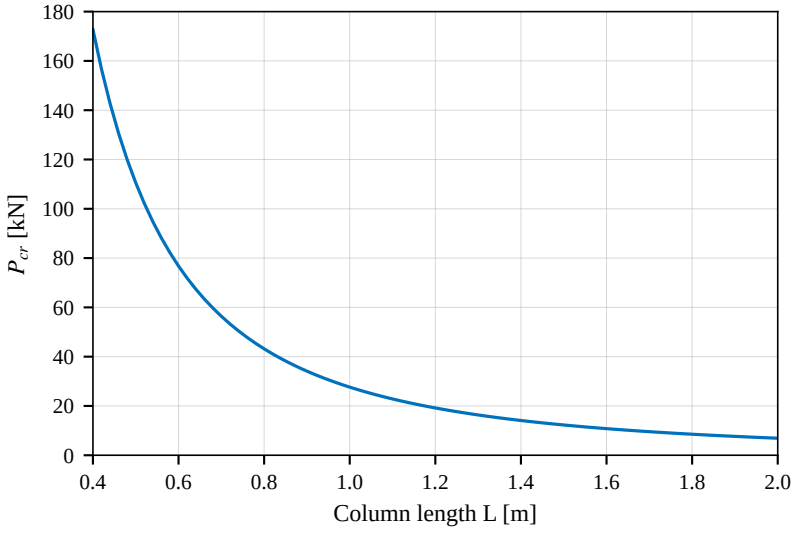


Fig. 3. Original MATLAB prediction of the inverse-square variation of the Euler critical load with column length

4.4. Energy-based stability of the column

Table 4 and Fig. 4 come from the original MATLAB archive and are samples of the analytical normalized stability indicator $1-P/P_{cr}$; they are not independent numerical verification. For a matrix-based check, $q(\alpha) = \varphi^{\mathrm{T}}(\mathbf{K}-\alpha\lambda_1\mathbf{K}_G)\varphi/(\varphi^{\mathrm{T}}\mathbf{K}\varphi)$ is also evaluated with the computed 40-element beam eigenvector. The separate audit CSV gives $q \approx +0.01, 0$, and -0.01 at $\alpha = 0.99, 1.00$, and 1.01. For an exact generalized eigenvector $q = 1-\alpha$, so this agreement verifies the assembled matrices and the eigenpair.

Table 4. Representative samples of the original analytical normalized stability-indicator sweep. The independent beam FE quadratic-form check is reported in the audit files

P/P_{cr}	Normalized curvature	State
0.000	1.000	Stable
0.500	0.500	Stable
0.900	0.100	Stable
0.990	0.010	Stable
0.995	0.005	Stable
1.000	0.000	Critical
1.005	-0.005	Unstable
1.100	-0.100	Unstable
1.300	-0.300	Unstable
1.500	-0.500	Unstable

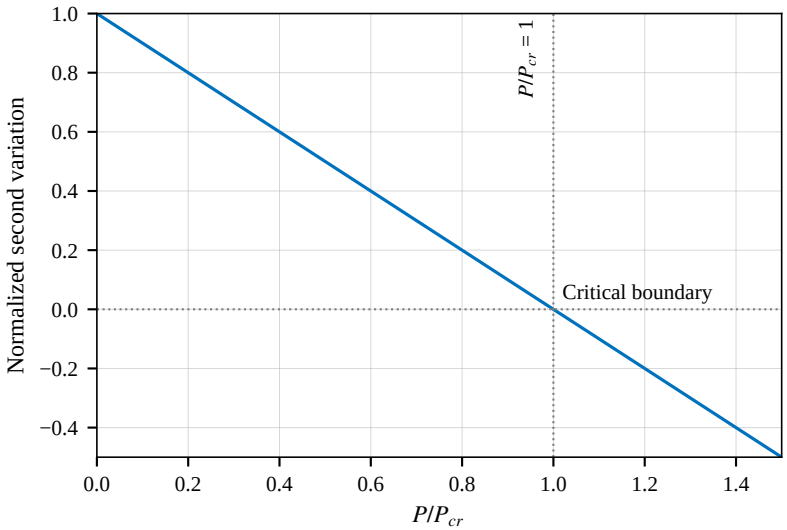


Fig. 4. Original MATLAB analytical stability-indicator curve for the compressed column; the FE matrix check is reported in the audit files

4.5. Initial imperfection amplification

For the prescribed initial amplitude $w_0 = 1$ mm, the linear secant relation $w_{max} = w_0/(1 - P/P_{cr})$ gives 2 mm at $P/P_{cr} = 0.5$, 10 mm at 0.9, and 20 mm at 0.95 (Table 5, Fig. 5). These points illustrate the assumed pre-critical relation; they are neither an independent finite-element result nor a post-buckling analysis. The expression is singular at $P = P_{cr}$ and cannot give a limit load or a post-buckling path, so the curve stops below the critical point.

Table 5. Representative values of the 1 mm initial-imperfection amplification curve

P/P_{cr}	Maximum deflection (mm)
0.000	1.000
0.250	1.333
0.500	2.000
0.700	3.333
0.800	5.000
0.850	6.667
0.900	10.000
0.925	13.333
0.950	20.000

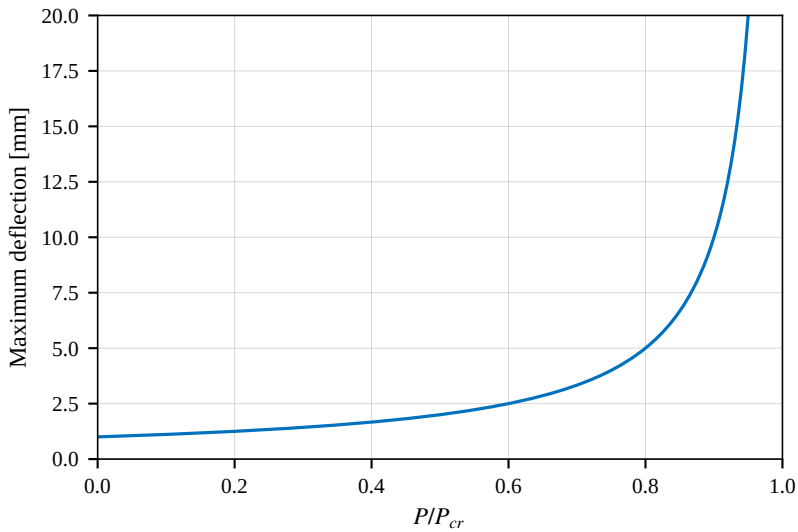


Fig. 5. Analytical pre-critical amplification of a prescribed 1 mm sinusoidal column imperfection; this secant relation is not a nonlinear post-buckling solution

4.6. Complete plate modal search and governing buckling pattern

The MATLAB plate calculation evaluates 32 admissible (m, n) combinations (Table 6, Fig. 6). The minimum occurs at (2,1), whose analytical sine surface appears in Fig. 7, followed by (1,1) and (3,1). The analytical and modal columns of this table rest on the same classical sinusoidal basis, so their near-zero differences are algebraic consistency checks, not independent finite-element validation. Independent numerical verification, with a Q4 mesh-convergence model and ANSYS SHELL181 solver output, follows in Section 4.7.

Table 6. Critical plate result for $a = 0.60$ m, $b = 0.40$ m, and $t = 4$ mm

a (m)	b (m)	t (mm)	D (N·m)	m	n	$N_{x,cr}$ (kN/m)	σ_{cr} (MPa)	Total edge load (kN)
0.600	0.400	4.000	1230.7692	2	1	329.5140	82.3785	131.8056

4.7. Independent numerical verification: Q4 and ANSYS SHELL181 convergence

The Q4 flat-shell calculation tests the classical plate result without reusing the sinusoidal trial basis. Its first eigenvalue falls monotonically from 373.960 kN/m on a 6×4 mesh to 329.645 kN/m on the 60×40 production mesh, against 329.514 kN/m from the classical Kirchhoff-Navier benchmark, a final difference of +0.0399% (Fig. 7a). The first numerical eigenvector is identified as $(m, n) = (2, 1)$, with a correlation essentially equal to one against the analytical sine mode (Fig. 7b). On the same mesh the next three identified longitudinal modes differ by +0.0540%, +0.1513%, and +0.3582% (Table 6a). A second mesh-refinement study, with the commercial SHELL181 element, follows.

Table 6a. Q4 flat-shell critical loads of the first four longitudinal modes on the 60×40 mesh (2400 elements) for $a = 0.60$ m, $b = 0.40$ m, and $t = 4$ mm, compared with the Kirchhoff-Navier values; Corr. is the correlation of the eigenvector with the analytical sine mode

No.	Mode (m, n)	FE $N_{x,cr}$ (kN/m)	Navier $N_{x,cr}$ (kN/m)	Error (%)	Corr.
1	(2,1)	329.645	329.514	+0.040	1.0000
2	(1,1)	356.595	356.402	+0.054	1.0000
3	(3,1)	475.218	474.500	+0.151	1.0000
4	(4,1)	704.908	702.392	+0.358	1.0000

The ANSYS SHELL181 study was carried out as a controlled structured refinement with 6×4, 12×8, 24×16, and 48×32 meshes (24, 96, 384, and 1536 shell elements; Figs. 7c and 7d). The first load multiplier drops from 154769.03 N to 132526.40 N. The reference load is a total 1 N edge compression, so $N_{x,cr} = F_{\mathrm{AC}}/b$ with $b = 0.40$ m, and the membrane loads are 386.923, 347.152, 335.562, and 331.316 kN/m. Against the Navier value of 329.514 kN/m, the errors fall from 17.422% to 5.353%, 1.835%, and 0.547%. Observed orders computed from the

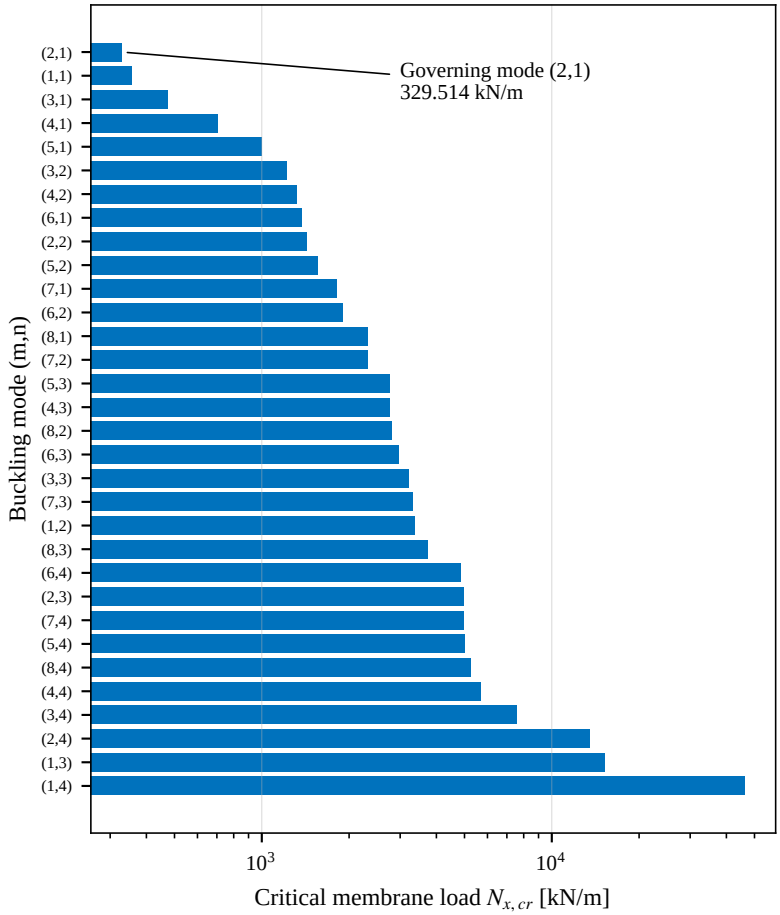


Fig. 6. Complete 32-mode plate candidate ranking reconstructed from the exported MATLAB modal table

analytical error with a directional refinement ratio of two are 1.703, 1.544, and 1.747. These are empirical rates for the complete APDL discretization, including the equal nodal partition of the reference edge load, and should not be read as a formal asymptotic interpolation order.

Table 6b. ANSYS SHELL181 structured mesh-convergence study for the first plate buckling mode

Mesh	Elements	FAC (N)	$N_{x,cr}$ (kN/m)	Error (%)	p_{obs}
6×4	24	154769.03	386.9226	+17.4222	—
12×8	96	138860.78	347.1520	+5.3527	1.7026
24×16	384	134224.81	335.5620	+1.8354	1.5442
48×32	1536	132526.40	331.3160	+0.5469	1.7469

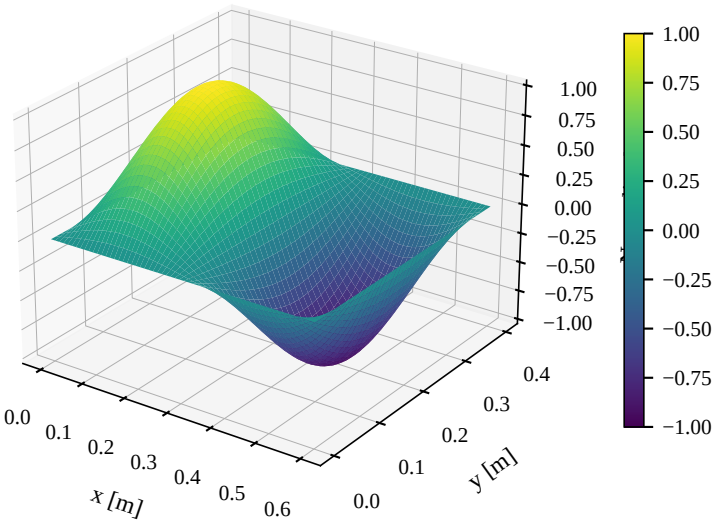


Fig. 7. Analytical admissible sine mode for the governing classical plate pattern $(m, n) = (2, 1)$; this surface is not an independently computed finite-element eigenvector

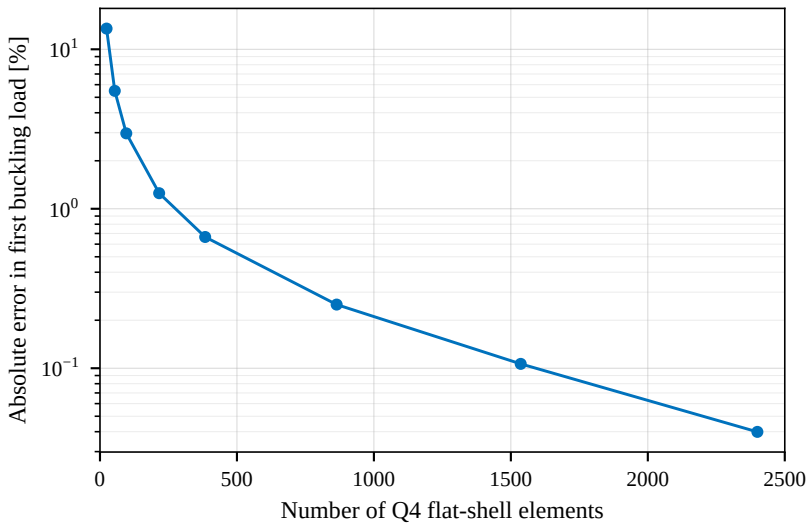


Fig. 7a. Mesh convergence of the Q4 flat-shell model; values are independent of the original modal-search CSV

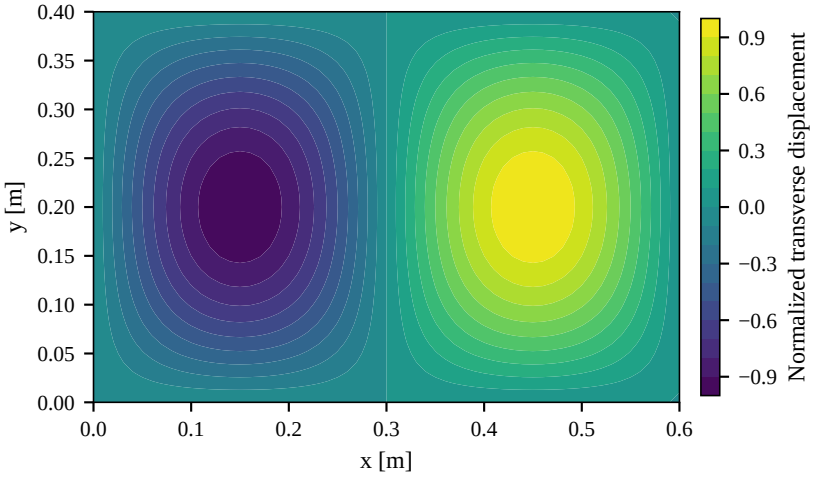


Fig. 7b. First Q4 flat-shell eigenvector on the 60×40 production mesh, identifying the (2,1) buckling pattern

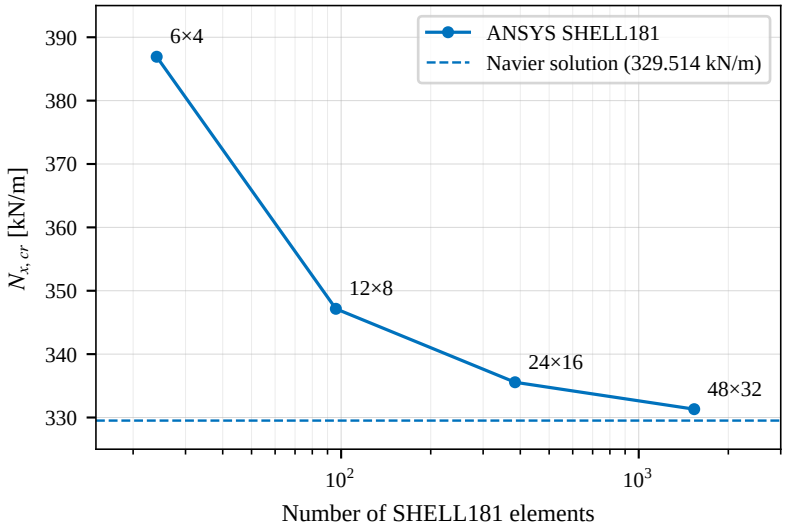


Fig. 7c. ANSYS SHELL181 convergence of the first plate buckling load for the structured 6×4, 12×8, 24×16, and 48×32 refinement sequence; the dashed reference is the classical Navier value $N_{x,cr} = 329.514$ kN/m

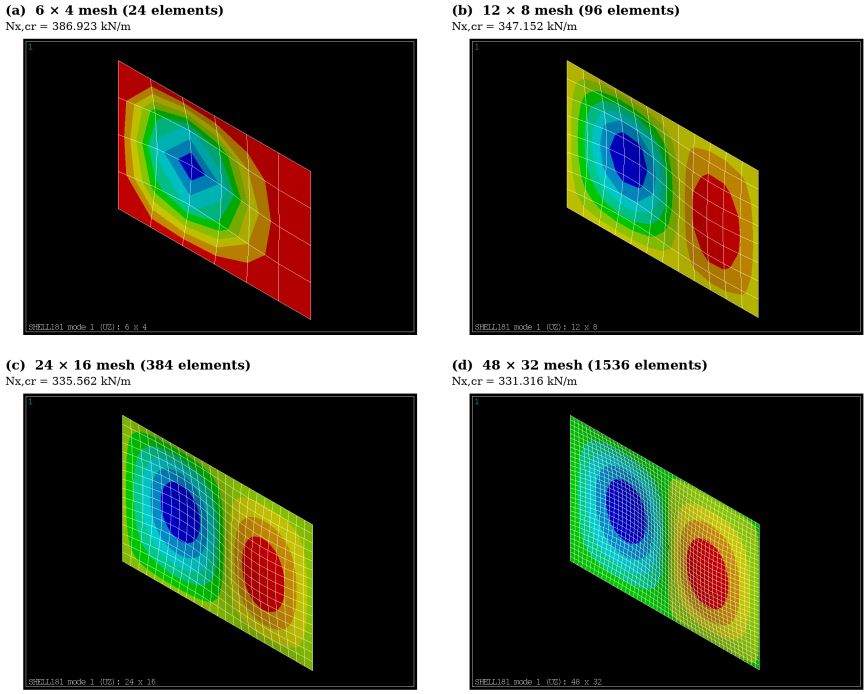


Fig. 7d. First ANSYS SHELL181 buckling eigenvector during structured mesh refinement: (a) 6×4, (b) 12×8, (c) 24×16, and (d) 48×32. The UZ contours preserve the governing (2,1) pattern while the critical load converges toward the Navier benchmark

A separate production-resolution ANSYS result is kept as an additional cross-check and is not inserted into the structured refinement sequence. The solver output reports 1080 SHELL181 elements, 6725 equations, Block Lanczos extraction of eight buckling eigenvectors, and first-four load multipliers of 131857.33, 142660.96, 190585.80, and 283857.33 N (Table 6c; mode shapes in Fig. 7e). With $b = 0.40$ m these correspond to 329.643, 356.652, 476.465, and 709.643 kN/m. Relative to the Navier values for the identified modes (2,1), (1,1), (3,1), and (4,1), the errors are +0.0392%, +0.0702%, +0.4140%, and +1.0324%. This run used the ESIZE-based meshing route and is therefore reported separately from the LESIZE-controlled convergence series above.

Note on the ANSYS boundary and load conditions. The SHELL181 decks behind Tables 6b and 6c constrain only UZ on the four edges (soft simple support) and split the 1 N reference load equally among all nodes of the loaded edge. Section 4.9.3 (Table 8e) quantifies both choices and shows that the equal partition is the main reason for the slow mesh convergence in Table 6b.

Table 6c. Independent ANSYS SHELL181 first-four-mode comparison using the 1080-element production-resolution solver output

Mode (m, n)	FAC (N)	ANSYS $N_{x,cr}$ (kN/m)	Navier $N_{x,cr}$ (kN/m)	Error (%)
(2,1)	131857.33	329.643	329.514	+0.0392
(1,1)	142660.96	356.652	356.402	+0.0702
(3,1)	190585.80	476.465	474.500	+0.4140
(4,1)	283857.33	709.643	702.392	+1.0324

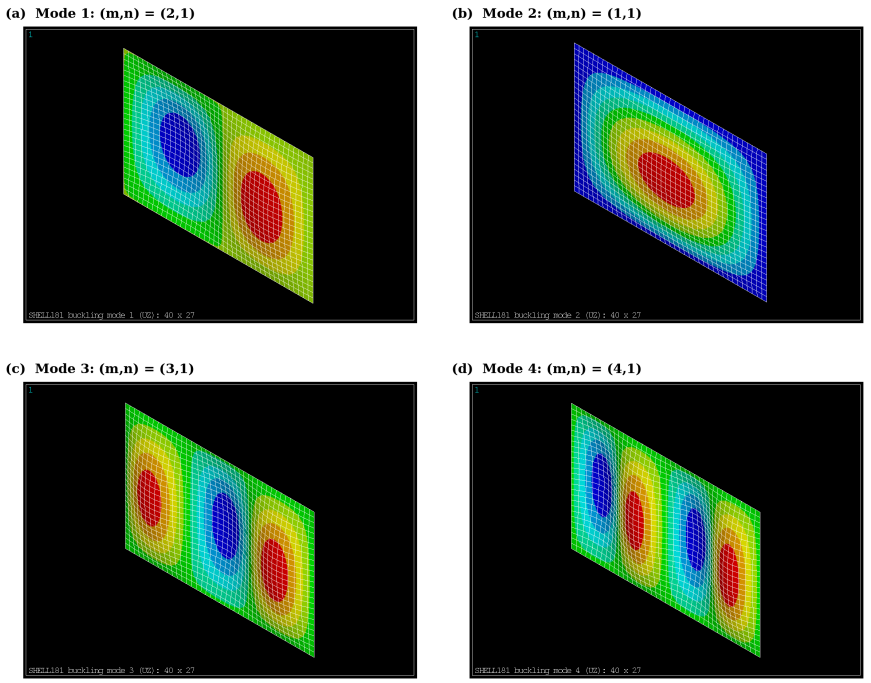


Fig. 7e. First four ANSYS SHELL181 production-resolution buckling eigenmodes: (a) (2,1), (b) (1,1), (c) (3,1), and (d) (4,1). The contours show normalized out-of-plane displacement UZ

4.8. Plate thickness sensitivity

The MATLAB thickness sweep (Table 7, Fig. 8) has 80 points from 1.5 to 8.0 mm, and the governing mode stays (2,1) throughout. Since $D \propto t^3$, the membrane buckling load scales as $N_{x,cr} \propto t^3$ and $\sigma_{cr} = N_{x,cr}/t$ as t^2. The complete 80-point dataset is kept in the Supplementary Data.

4.9. Aspect ratio sensitivity and mode transitions

The aspect-ratio sweep (Fig. 9) has 101 points between $r = a/b = 0.50$ and 3.00 in steps of 0.025. Throughout, $b = 0.40$ m, $t = 4$ mm, $E = 210$ GPa,

Table 7. Representative values from the complete 80-point plate-thickness sweep

Thickness (mm)	$N_{x,cr}$ (kN/m)	Critical stress (MPa)	m
1.500	17.377	11.584	2
2.241	57.907	25.846	2
3.063	147.999	48.314	2
3.886	302.154	77.753	2
4.709	537.578	114.163	2
5.532	871.479	157.544	2
6.354	1321.064	207.897	2
7.177	1903.539	265.220	2
8.000	2636.112	329.514	2

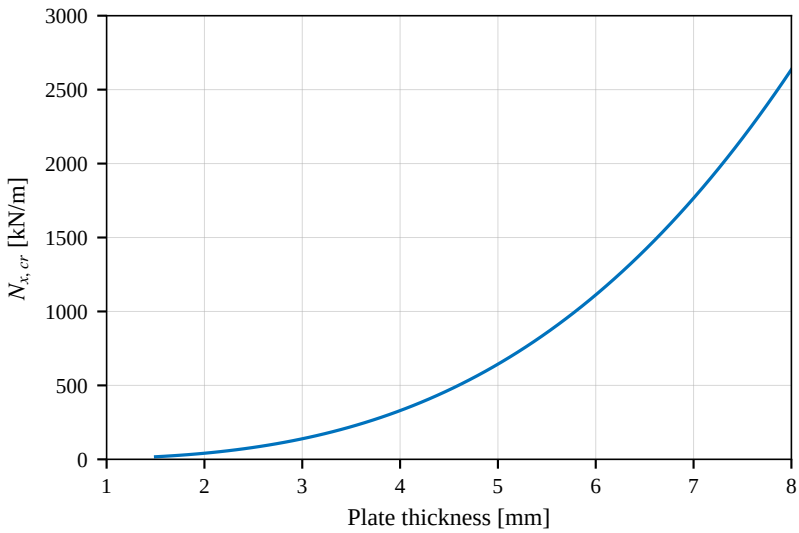


Fig. 8. Original MATLAB thickness-sensitivity curves for plate critical membrane load and critical stress

and $\nu = 0.30$ are fixed while $a = rb$ varies. The critical transverse mode stays $n = 1$, whereas the longitudinal mode changes from $m = 1$ to $m = 2$ and then to $m = 3$. The sampled transition brackets are 1.400–1.425 and 2.425–2.450 (Table 8, Fig. 10), and the classical tie points $\sqrt{2} \approx 1.41421356$ and $\sqrt{6} \approx 2.44948974$ lie inside them.

Table 8. Governing plate-mode intervals extracted from the complete aspect-ratio sweep

Resolved a/b interval	Critical m	Critical n	Data points
0.500–1.400	1	1	37
1.425–2.425	2	1	41
2.450–3.000	3	1	23

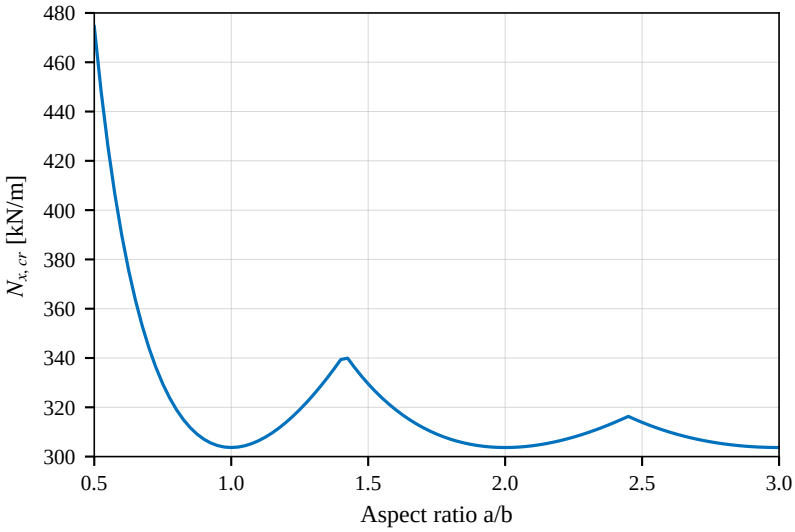


Fig. 9. Original MATLAB variation of plate critical load and stress with aspect ratio

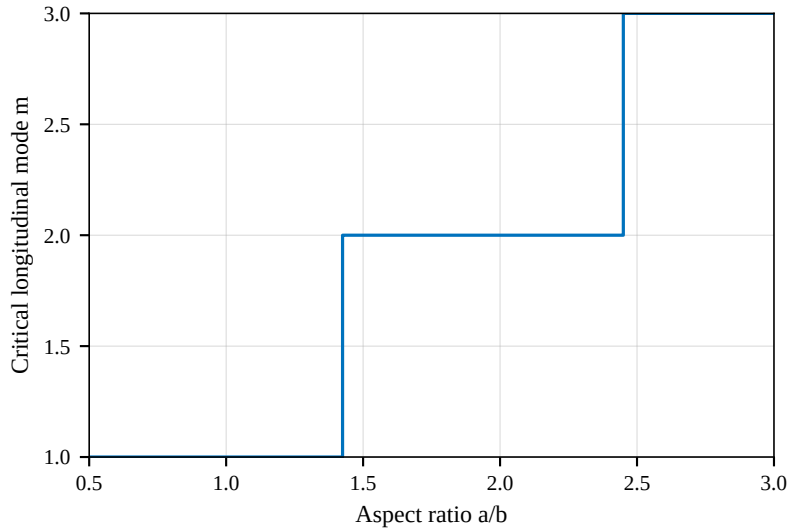


Fig. 10. Original MATLAB mode-selection map showing changes in the governing longitudinal half-wave number

The mechanism behind these mode changes is the dimensionless coefficient $k_m = (m/r + r/m)^2$: the governing solution is the lower envelope of the competing integer-mode branches, and adjacent branches intersect exactly at $r = \sqrt{m(m+1)}$. This gives an analytical mode-selection map instead of a purely sampled one.

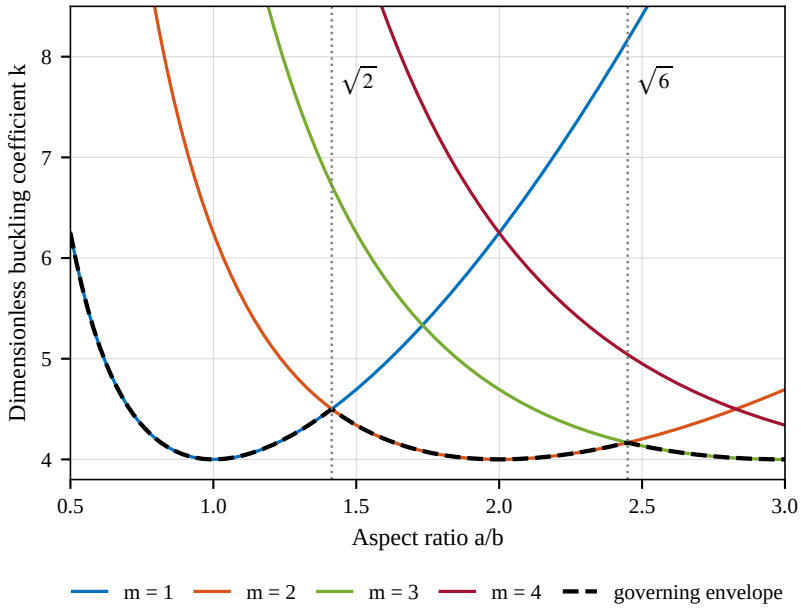


Fig. 11. Analytical competition among longitudinal plate modes and exact mode-transition boundaries; the dashed lower envelope defines the governing buckling coefficient

4.9.1. Numerical localization of double-eigenvalue mode transitions

The Q4 eigenproblem was used to find where adjacent longitudinal branches exchange order. Multiple eigenvalues are a recognized spectral issue in plate buckling [13, 14]. The exact crossings serve as references, and the question is how quickly an independent finite-element discretization recovers them. For each transition $b = 0.40$ m, $t = 4$ mm, $E = 210$ GPa, and $\nu = 0.30$ are fixed while $a = rb$. Branch identity follows from the correlation of each Q4 eigenvector with $\sin(m\pi x/a)\sin(\pi y/b)$. The zero of $\Delta m(r) = N_{x,FE}(m,1) - N_{x,FE}(m+1,1)$ is estimated from bracketing evaluations and then checked by recomputing the branch-gap residual at the estimated crossing.

The localization error decreases steadily with refinement (Fig. 11a). On the finest meshes the first crossing is recovered at $r = 1.41426388$, only 5.03×10^{-5} in aspect ratio (0.00356%) above $\sqrt{2}$, and the second at $r = 2.45021557$, 7.26×10^{-4} (0.0296%) above $\sqrt{6}$. At these estimates the residual separation of the two tracked

Table 8a. Finite-element localization of the first two classical plate mode-transition aspect ratios. Errors are relative to the thin-plate (Kirchhoff) values; the shear-corrected (Mindlin) references are given in Section 4.9.2

Mode pair	Q4 mesh	Elements	r_{FE}	r_{exact}	Error (%)
1↔2	12×8	96	1.421992	1.414214	0.5500
1↔2	24×16	384	1.415773	1.414214	0.1102
1↔2	48×32	1536	1.414264	1.414214	0.00356
2↔3	20×8	160	2.460841	2.449490	0.4634
2↔3	39×16	624	2.452192	2.449490	0.1103
2↔3	59×24	1416	2.450216	2.449490	0.02963

branches is below 5×10^{-6} kN/m, and each branch keeps essentially unit correlation with its sine-mode family. Because the Q4 element includes transverse shear, however, the classical crossings are not its convergence targets: the very small error of the first crossing relative to $\sqrt{2}$ is partly a cancellation between a positive discretization error and a negative shear-induced shift of the crossing (Section 4.9.2).

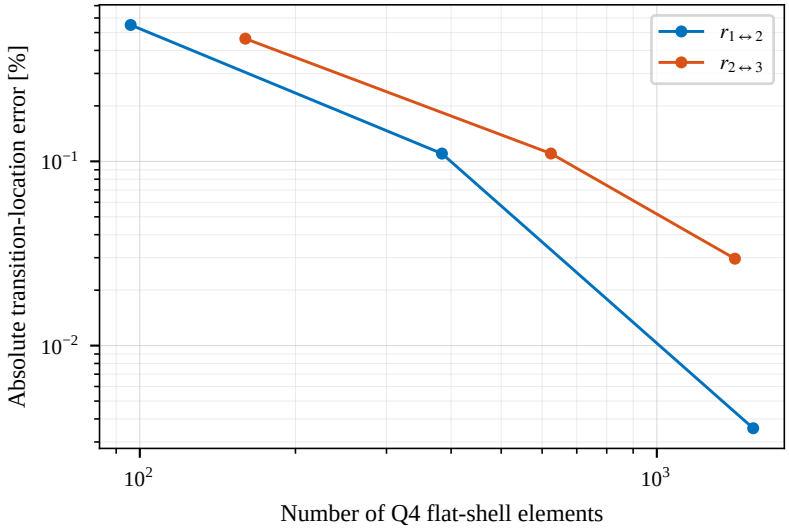


Fig. 11a. Mesh-dependent error in Q4 localization of the first two classical double-eigenvalue mode-transition points; $\sqrt{2}$ and $\sqrt{6}$ are used only as reference locations

4.9.2. Shear-induced shift of the transition points and re-referenced localization

Because the Q4 and SHELL181 models include transverse shear, their crossings converge to the Mindlin values of Eq. (31a) and not to $\sqrt{m(m+1)}$. To test this, the localization was repeated for $b/t = 20$, 50, 100, and 200 (Q4) and $b/t = 20$,

50, and 100 (SHELL181), with $b = 0.40$ m, $E = 210$ GPa, $\nu = 0.30$, $\kappa = 5/6$, and the meshes of Table 8a. The Q4 crossings were located as in Section 4.9.1. For SHELL181, the two lowest eigenvalues were computed at $r = r^*(1 + \delta)$ with $\delta = -1.5, -0.6, +0.6$, and $+1.5\%$. The branches were assigned by the side of the crossing (the lower branch is $(m, 1)$ for $r < r^*$ and $(m + 1, 1)$ for $r > r^*$), quadratic fits were made for both, and their intersection was taken as r_{FE}. Applied to Q4 data, this procedure reproduces the secant results of Section 4.9.1 to about 10^{-6} in r. The SHELL181 decks use hard simple support (UZ = 0 on all edges, ROTX = 0 on $x = 0$ and $x = a$, ROTY = 0 on $y = 0$ and $y = b$), as in the Q4 model, and a consistent edge load with half the nodal load at the two corner nodes.

Table 8b. Transition aspect ratios: thin-plate (Kirchhoff) values, Mindlin values from Eq. (31a), and finest-mesh Q4 and SHELL181 results (48×32 for 1↔2, 59×24 for 2↔3). A dash means that no SHELL181 run was made for that b/t

b/t	Pair	Kirchhoff	Mindlin	Shift (%)	Q4	SHELL181
20	1↔2	1.414214	1.403042	-0.790	1.403525	1.403272
20	2↔3	2.449490	2.431568	-0.732	2.432978	2.432183
50	1↔2	1.414214	1.412420	-0.127	1.412917	1.412658
50	2↔3	2.449490	2.446613	-0.117	2.448055	2.447243
100	1↔2	1.414214	1.413765	-0.032	1.414264	1.414004
100	2↔3	2.449490	2.448770	-0.029	2.450216	2.449402
200	1↔2	1.414214	1.414101	-0.008	1.414601	–
200	2↔3	2.449490	2.449310	-0.007	2.450757	–

Table 8c. Error of the finest-mesh crossing relative to the Kirchhoff and Mindlin references (%). A dash means that no SHELL181 run was made for that b/t

b/t	Pair	Q4 vs. Kirchhoff	Q4 vs. Mindlin	SHELL181 vs. Kirchhoff	SHELL181 vs. Mindlin
20	1↔2	-0.756	+0.034	-0.774	+0.016
20	2↔3	-0.674	+0.058	-0.707	+0.025
50	1↔2	-0.092	+0.035	-0.110	+0.017
50	2↔3	-0.059	+0.059	-0.092	+0.026
100	1↔2	+0.004	+0.035	-0.015	+0.017
100	2↔3	+0.030	+0.059	-0.004	+0.026
200	1↔2	+0.027	+0.035	–	–
200	2↔3	+0.052	+0.059	–	–

Tables 8b and 8c and Figs. 11b and 11c summarize the results, which lead to three observations. First, both independent models converge to the Mindlin crossing. At $b/t = 20$ the finest-mesh crossings lie 0.76% (Q4) and 0.77% (SHELL181) below $\sqrt{2}$, which is 20 to 50 times the corresponding discretization error measured against the Mindlin value. A reference-free Richardson extrapolation of the three meshes of the 1↔2 transition (observed order 2.04 for Q4 and 2.06 for SHELL181) gives 1.403057 and 1.403051 at $b/t = 20$, 1.412436 and 1.412430 at $b/t = 50$,

and 1.413781 and 1.413775 at $b/t = 100$, which agree with Eq. (31a) to within 11 and 7 parts per million, respectively. Second, the discretization error is nearly independent of b/t. For Q4, it is 0.58%, 0.14%, and 0.035% on the three meshes of the first crossing for every b/t, that is, second order, while the physical shift varies as $(t/b)^2$. The small error relative to $\sqrt{2}$ reported in Section 4.9.1 is therefore partly a cancellation: at $b/t = 100$ the SHELL181 crossings on the finest meshes lie below $\sqrt{2}$ and $\sqrt{6}$ (−0.015% and −0.004%) even though the actual discretization error relative to the Mindlin values is positive (+0.017% and +0.026%). Third, the second crossing converges less regularly (observed order 1.7 to 2.2) because the 20×8, 39×16, and 59×24 meshes are not geometrically similar, so finest-mesh errors rather than extrapolated limits are quoted for the 2 ↔ 3 transition.

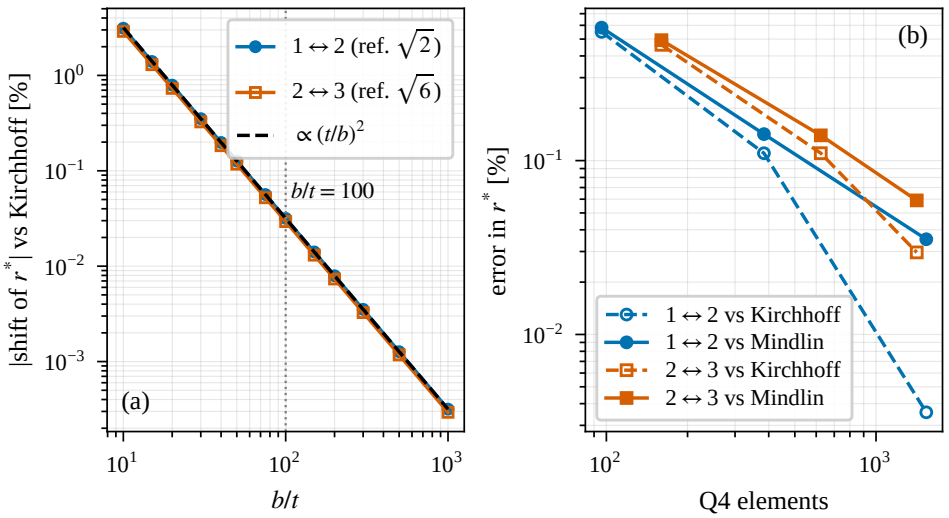


Fig. 11b. (a) Shear-induced shift of the transition aspect ratios versus b/t for $\kappa = 5/6$; the dashed line is proportional to $(t/b)^2$. (b) The Q4 localization errors of Table 8a re-referenced to the Kirchhoff and Mindlin values

Mode-misidentification band. For a mesh whose crossing estimate is r_{FE}, the lower-load mode is identified wrongly for aspect ratios between r^* and r_{FE}. At $b/t = 100$ the width $\Delta r = r_{FE} - r^*$ (Mindlin) of this band is 8.2×10^{-3}, 2.0×10^{-3}, and 5.0×10^{-4} for the three Q4 meshes of the 1↔2 transition (96, 384, and 1536 elements) and 4.0×10^{-3}, 9.6×10^{-4}, and 2.4×10^{-4} for SHELL181. For the 2↔3 transition the Q4 values are 1.2×10^{-2}, 3.4×10^{-3}, and 1.4×10^{-3} and the SHELL181 values 4.6×10^{-3}, 1.6×10^{-3}, and 6.3×10^{-4}. The band narrows roughly as h^2, so a required band width fixes the mesh density needed for a given element family. Inside the band the predicted governing pattern is wrong, although the load difference between the two competing branches vanishes at r^*.

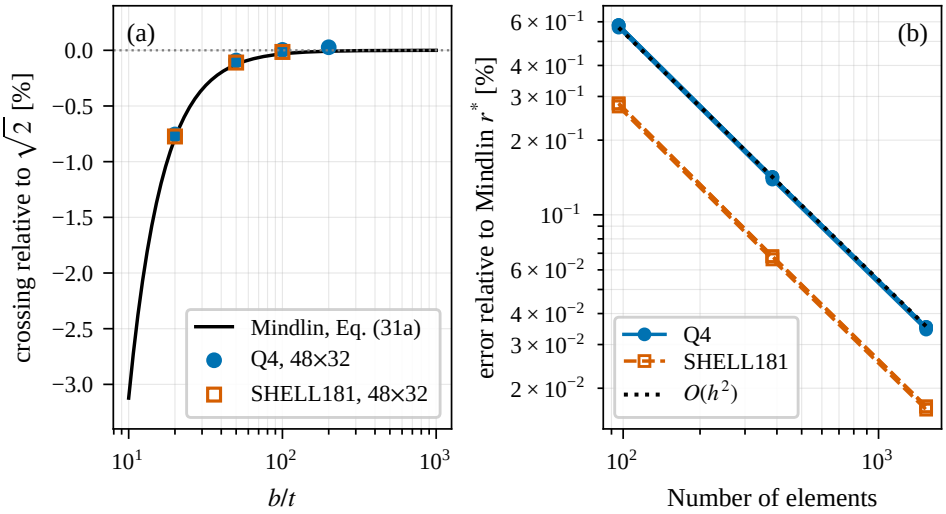


Fig. 11c. (a) Finest-mesh first crossing relative to $\sqrt{2}$ versus b/t for Q4 and SHELL181 compared with the Mindlin curve of Eq. (31a). (b) Convergence of the first crossing toward the Mindlin value for several b/t; the dotted line is proportional to h^2

4.9.3. Support-condition and load-introduction sensitivity of the SHELL181 reference

The ANSYS decks of Section 4.7 constrain only UZ on the four edges (rotations free, soft simple support) and split the 1 N reference edge load equally among all nodes of the loaded edge, corner nodes included. The Mindlin solution of Eq. (31a) and the Q4 model enforce the tangential rotation instead (hard simple support). The two conditions are equivalent in Kirchhoff theory but not in shear-deformable models. The modified decks (supplementary folder) impose ROTX = 0 on $x = 0$ and $x = a$ and ROTY = 0 on $y = 0$ and $y = b$, apply a consistent edge load in which the corner nodes carry half the nodal load, and include a soft-support switch. Table 8d compares the first buckling load for $a/b = 1.5$, $b/t = 100$, and a 60×40 mesh.

Table 8d. First buckling load $N_{x,cr}$ (kN/m) for $a/b = 1.5$, $b/t = 100$, and 60×40 elements with hard and soft simple support

Support condition	Q4	SHELL181	Mindlin, Eq. (31a)	Kirchhoff
Hard ($\psi_t = 0$)	329.645	329.714	329.256	329.514
Soft (ψ_t free)	328.748	328.818	–	–

Soft support lowers the load by 0.272% in both models at 60×40, and the two programs differ by 0.021% for either support condition. In the Q4 model, soft support leaves the crossing unchanged at $b/t = 100$ ($r_{FE} = 1.414264$ on 48×32) and moves it by +0.05% at $b/t = 20$ (1.404216 versus 1.403525). The effect of the

load-introduction scheme was isolated in a 2×2 test at $a/b = 1.5$ and $b/t = 100$ (SHELL181, 24×16 and 48×32 elements) in which only the support condition and the nodal load distribution changed (Table 8e). The run with soft support and equal partition on 48×32 reproduces the value of Table 6b (331.316 kN/m) exactly.

Table 8e. SHELL181 first buckling load $N_{x,cr}$ (kN/m) at $a/b = 1.5$ and $b/t = 100$ for the old (equal nodal partition) and the consistent edge load, with soft and hard simple support

Mesh	Support	Equal partition	Consistent load	Change (%)
24×16	Soft	335.562	331.754	-1.135
24×16	Hard	335.951	332.139	-1.135
48×32	Soft	331.316	329.234	-0.628
48×32	Hard	332.058	329.972	-0.628

Two results follow. First, the load-introduction scheme changes the load by the same relative amount for both support conditions (−1.135% on 24×16, −0.628% on 48×32), and this change falls by a factor of 1.83 when the mesh is doubled. In other words, the equal nodal partition, which loads the two corner nodes as heavily as the interior edge nodes, introduces a first-order error. Of the 2.57 kN/m by which the 48×32 value of Table 6b exceeds the Q4 value for soft support (328.748 kN/m), 2.08 kN/m (81%) is due to this scheme. With the consistent load and hard support, the error relative to the Mindlin value of 329.256 kN/m is +0.88%, +0.22%, and +0.14% on 24×16, 48×32, and 60×40 (Table 8d), an observed order of 2.0 between the first two meshes, whereas with the equal partition it is +2.03% and +0.85% (order 1.3). The slow convergence of the structured SHELL181 sequence in Table 6b thus comes mainly from the load application, not from the element. Second, the difference between hard and soft support depends on the mesh in SHELL181 (0.116%, 0.224%, and 0.272% on 24×16, 48×32, and 60×40) and tends to the Q4 value of 0.272%. The agreement between the 1080-element SHELL181 value (329.643 kN/m) and the Q4 value (329.645 kN/m) is therefore partly fortuitous: that deck used soft support, which alone lowers the load by about 0.27% relative to hard support, and a different meshing route.

4.10. Poisson ratio sensitivity

For fixed $E, t, a/b$, and modal indices, Poisson's ratio enters the classical buckling load only through D, and the factor $1/(1-\nu^2)$ grows monotonically relative to $\nu = 0$. For the present plate, $N_{x,cr}$ rises from 299.858 kN/m at $\nu = 0$ to 329.514 kN/m at $\nu = 0.30$ and 394.602 kN/m at $\nu = 0.49$, an increase of about 31.6% from $\nu = 0$ to 0.49. The effect is moderate next to the cubic thickness dependence, but it is systematic and should not be ignored when comparing materials with very different Poisson ratios.

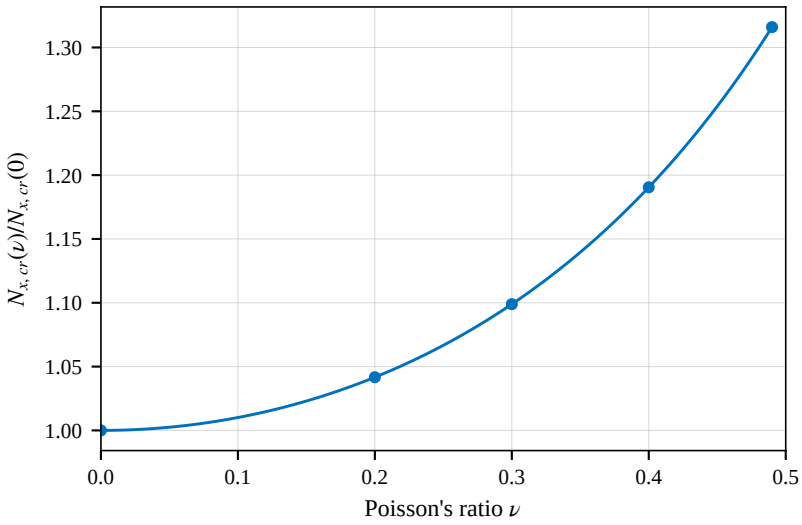


Fig. 12. Closed-form sensitivity of the plate buckling load to Poisson's ratio, normalized by the $\nu = 0$ value

4.11. Energy-based stability of the plate

Table 9 and the corresponding original curve are samples of the analytical plate indicator $1 - N_x/N_{x,cr}$, not independent numerical data. The flat-shell model supplies a separate matrix check through $q(\alpha) = \varphi^{\mathrm{T}}(\mathbf{K} - \alpha\lambda_1\mathbf{K}_G)\varphi/(\varphi^{\mathrm{T}}\mathbf{K}\varphi)$, and its supplementary CSV gives $q \approx +0.01$, 0, and -0.01 at $\alpha = 0.99$, 1.00, and 1.01.

Table 9. Representative samples of the original analytical plate stability-indicator sweep; the independent flat-shell quadratic-form check is reported in the supplementary files

$N_x/N_{x,cr}$	Normalized curvature	State
0.000	1.000	Stable
0.500	0.500	Stable
0.900	0.100	Stable
0.990	0.010	Stable
0.995	0.005	Stable
1.000	0.000	Critical
1.005	-0.005	Unstable
1.100	-0.100	Unstable
1.300	-0.300	Unstable
1.500	-0.500	Unstable

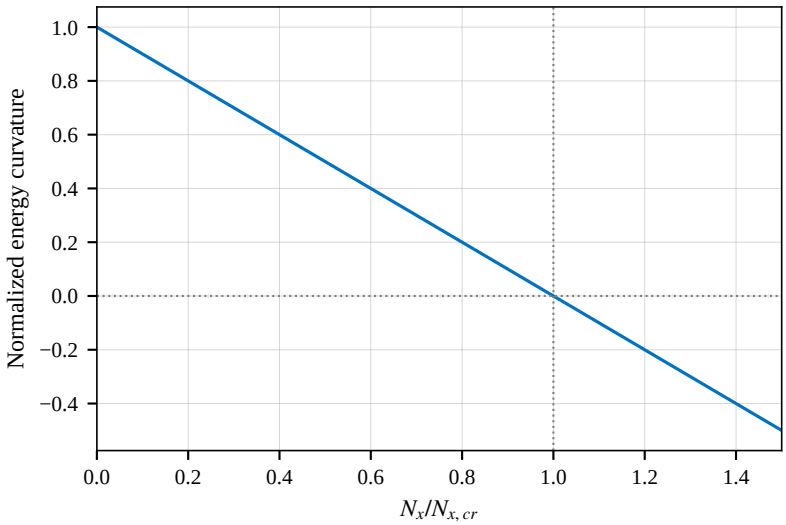


Fig. 13. Original analytical normalized plate stability indicator; independent flat-shell matrix values around the first eigenvalue are provided in the supplementary data

4.12. Reproducibility of results

Table 10 lists the MATLAB-derived result groups and the main reproducibility routes. The project archive holds the generator RUN_BUCKLING_STABILITY_STUDY.m, the MAT/CSV/PNG result files, and ANSYS APDL reproduction decks for the BEAM188 and SHELL181 models. The supplementary package adds a SHELL181 mesh-convergence subfolder with the executed 6×4, 12×8, 24×16, and 48×32 text outputs, matrix files, mesh and mode PNG exports, the APDL convergence deck, and a derived convergence CSV. The 1080-element production-resolution solver products and first-four mode images are included with them. Q4 mesh convergence is in flat_shell_validation and the audit files are in audit. The Mindlin-reference study of Sections 2.8 and 4.9.2 to 4.9.3 adds the MATLAB and APDL sources and the result tables listed in the Data Availability statement.

4.13. Higher-order beam verification: Euler-Bernoulli versus Timoshenko theory

A Timoshenko beam comparison quantifies how transverse shear deformation affects the elastic buckling load of the simply supported column. The Euler-Bernoulli formulation remains the slender-column reference. The Timoshenko result is a closed-form shear-flexibility correction to the Euler-Bernoulli load [1, 2], not a finite-element calculation, and rotary inertia plays no role because the problem is static buckling.

The comparison covers a range of slenderness ratios L/h with the same material and boundary conditions as the reference model (Table 11). The two theories

Table 10. Original archived MATLAB-derived result groups and their reproducibility routes

Result group	Rows	Original archived numerical export	Figure / source
Column buckling modes	4	column_buckling_ modes.csv	column_buckling_ modes.png
Column mesh convergence	7	column_mesh_ convergence.csv	column_mesh_ convergence.png
Column length sensitivity	81	column_length_ sensitivity.csv	column_length_ sensitivity.png
Column energy stability	301	column_stability_ energy.csv	column_energy_ stability.png
Column imperfection amplification	191	column_imperfection_ amplification.csv	column_imperfection_ amplification.png
Plate buckling candidates	32	plate_buckling_ candidates.csv	Figure 6 reconstructed
Plate critical summary	1	plate_critical_summary.csv	plate_critical_mode.png
Plate thickness sensitivity	80	plate_thickness_ sensitivity.csv	plate_thickness_ sensitivity.png
Plate aspect-ratio sensitivity	101	plate_aspect_ratio_ sensitivity.csv	plate_aspect_ratio_ sensitivity.png
Plate mode transitions	101	plate_aspect_ratio_ sensitivity.csv	plate_critical_mode_vs_ aspect_ratio.png
Plate energy stability	301	plate_stability_energy.csv	Fig. 13 (reconstructed)
Exact plate mode-transition map	Analytical	Closed-form expression	Fig. 11
Poisson-ratio sensitivity	Analytical	Closed-form expression	Fig. 12
Original MATLAB generator	Source	RUN_BUCKLING_ STABILITY_STUDY.m	Generates archived MAT/CSV/PNG outputs
ANSYS column input deck	Input	ANSYS_COLUMN_ EIGENVALUE_ BUCKLING.mac	BEAM188 reproduction route; input deck only, no solver output included
ANSYS plate reproduction deck	Input	ANSYS_PLATE_ EIGENVALUE_ BUCKLING.mac	SHELL181 reproduction route accompanying recovered plate solver evidence
ANSYS plate solver validation	Raw output	plate_SHELL181_ validation1.out + .rst/.mode/.full + mode1-4.png	Executed 2021 R1 SHELL181 cross-check; 1080 elements, 8 extracted modes

coincide for high slenderness, while the Timoshenko load falls increasingly below the Euler-Bernoulli load as the member gets shorter and shear deformation matters more. The difference, defined as $(P_{cr,EB} - P_{cr,T})/P_{cr,EB}$, varies as $(L/h)^{-2}$ and is 2.50% at $L/h = 10$, 0.637% at $L/h = 20$, 0.102% at $L/h = 50$, 0.0257% at $L/h = 100$, and 0.0064% at $L/h = 200$. For the slender column of the main benchmark, the shear correction is negligible. The dataset, script, and figures of this comparison are in the supplementary package.

Table 11. Euler-Bernoulli and Timoshenko buckling loads (N) of the simply supported column for several slenderness ratios L/h

L/h	Euler-Bernoulli P_{cr} (N)	Timoshenko P_{cr} (N)	Difference (%)
10	690,872.3	673,587.4	2.50
20	172,718.1	171,617.1	0.637
50	27,634.9	27,606.6	0.102
100	6,908.7	6,907.0	0.0257
200	1,727.2	1,727.1	0.0064

5. Discussion

The near-perfect agreement between the Euler solution and the beam finite-element model validates the implementation of the elastic and geometric stiffness matrices, the simply supported boundary conditions, and the generalized eigenvalue procedure. The convergence study shows that the agreement is not accidental: the error falls steadily under uniform refinement and the observed order approaches four. Accurate first-mode predictions therefore need only a modest number of cubic beam elements.

Higher-mode errors are larger than the first-mode error, though still very small. The higher eigenmodes are more oscillatory, and a fixed mesh resolves the smooth first mode better than modes with several half-waves.

The energy criterion gives the eigenvalue results a physical meaning. Below the critical load a small enough lateral perturbation raises the total potential energy, and the column tends to return to the straight configuration. At the critical load the quadratic energy coefficient vanishes, and above it a perturbation can lower the total potential energy, so the straight state is unstable.

The imperfection analysis demonstrates why ideal eigenvalue buckling loads must be interpreted cautiously. The linear amplification relation becomes singular as P/P_{cr} approaches unity. Real columns do not develop infinite displacement; geometric nonlinearity, material nonlinearity, residual stresses, and boundary imperfections regulate the response. The amplification equation should therefore be treated as a pre-critical sensitivity indicator rather than a post-buckling constitutive law.

For the plate, the modal solution captures the dependence of the governing buckling pattern on aspect ratio. At $a/b = 1.5$, the minimum load corresponds to two longitudinal half-waves. This confirms the importance of minimizing over several admissible modal integers instead of assuming a single deformation pattern.

The classical mode-transition relation is used here as a benchmark. For $n = 1$, $k_m(r) = (m/r + r/m)^2$, and adjacent branches meet at $r = \sqrt{m(m+1)}$, where the two modes tie as a double eigenvalue. The original MATLAB aspect-ratio sweep only brackets these points. The Q4 localization test asks a different, numerical question: how accurately does an independent discrete spectrum recover the known crossings? Refinement reduces the $r_{1\leftrightarrow 2}$ error from 0.5500% on 12×8 elements to

0.00356% on 48×32 elements, and the $r_{2\leftrightarrow 3}$ error from 0.4634% on 20×8 elements to 0.0296% on 59×24 elements. This test is more demanding than reproducing a single critical load because it needs correct branch identity and resolution of nearly coincident eigenvalues.

The shear-deformable models used for the numerical checks converge not to the thin-plate crossings but to the Mindlin values of Eq. (31a), which lie below them by 0.03% at $b/t = 100$ and 0.8% at $b/t = 20$ for the first transition (Section 4.9.2). The localization errors quoted above relative to $\sqrt{2}$ and $\sqrt{6}$ therefore mix a positive discretization error with a negative physical shift. Relative to the Mindlin references, the finest-mesh errors are +0.035% (Q4) and +0.016% (SHELL181) for the first crossing at b/t between 20 and 100.

Practical implications. For $b/t \geq 100$, choosing the number of half-waves from $a/b = \sqrt{m(m+1)}$ is accurate to better than 0.03% in aspect ratio, which is below the localization error of a shell model with about 10^3 elements. For stockier plates, the transition occurs at smaller aspect ratios than the thin-plate rule predicts: by 0.13% at $b/t = 50$, 0.35% at $b/t = 30$, and 0.8% at $b/t = 20$ for the first transition. Near a transition, the two competing modes carry nearly the same load, so the load hardly depends on the choice, but the buckling pattern does, and with it the stiffener spacing or the imperfection shape to be assumed. A sufficiently fine shell-element check is then advisable. With the present Q4 family, about 100, 400, and 1500 elements keep the band of governing-mode misidentification within ±0.6%, ±0.14%, and ±0.035% of the first transition at $b/t = 100$.

Poisson's ratio has a weaker but analytically transparent influence. The critical load is proportional to $(1-\nu^2)^{-1}$, so its logarithmic sensitivity equals $2\nu^2/(1-\nu^2)$, about 0.198 at $\nu = 0.30$, whereas thickness enters cubically. Thickness is therefore the dominant geometric stiffness parameter in this isotropic benchmark, and ν matters mainly in cross-material comparisons or inverse identification studies.

This verification hierarchy follows current computational practice, in which classical solutions serve as controlled benchmarks for discretization, convergence, boundary-condition enforcement, eigenmode identification, and spectral multiplicity before more complex constitutive or geometric models are introduced [11–18, 24–26]. The benchmark is deliberately simple. Its educational value comes from combining archived evidence, explicit beam convergence reporting, independent Q4 and ANSYS refinement studies, and the transition-localization experiment that turns the known double-eigenvalue aspect ratios into quantitative FE error targets.

The analytical sweeps, including the plate modal sweep, which uses the same sinusoidal admissible basis as the closed-form solution, are consistency checks only. Independent numerical verification comes from the Q4 flat-shell model, with its own spatial discretization, mesh-convergence sequence, boundary-condition implementation, and mode-shape identification, and from the ANSYS SHELL181 refinement series.

Both refinement studies approach the same classical Navier benchmark through different finite-element implementations. Their limitations are those of ideal linear eigenvalue analysis: they do not represent measured geometric imperfections, residual stresses, plasticity, or a nonlinear equilibrium path, which call for a separate nonlinear or experimental study.

6. Limitations and future work

The study is restricted to ideal linear elastic bifurcation. Materials are homogeneous, isotropic, and linearly elastic; the column follows Euler-Bernoulli theory, and the analytical plate benchmark follows classical thin-plate theory. The numerical plate checks are an in-house Q4 Reissner-Mindlin flat-shell model with MITC-type shear tying and ANSYS SHELL181 eigenvalue-buckling calculations. The benchmark plate has $b/t = 100$, so the classical thin-plate solution is still an appropriate reference. The transverse-shear effect is small at this thickness (0.078% in the load and 0.03% in the transition aspect ratios) but not negligible for thicker plates (0.8% in the first transition at $b/t = 20$), and it is of the same order as the finite-element localization errors of Section 4.9.1. Residual stresses, yielding, manufacturing defects, load eccentricity, imperfect supports, and nonlinear post-buckling response are left out.

The shear-deformation results depend on a shear-correction factor $\kappa = 5/6$ (explicit in the Q4 element and assumed for SHELL181), on hard simple support, on isotropic material, and on uniaxial compression. The load-introduction test of Section 4.9.3 covers a single geometry ($a/b = 1.5$, $b/t = 100$) and two meshes, and the second crossing converges less regularly because its meshes are not geometrically similar.

Future work should extend the framework to geometrically nonlinear analysis with measured or prescribed imperfections. Nonlinear limit loads and post-buckling paths lie outside the present linear analysis. Arc-length or displacement-controlled procedures could trace stable and unstable post-buckling branches. Other directions include nonuniform columns, rotational end restraints, Timoshenko beam finite elements, nonlocal elasticity theories, orthotropic and laminated composite plates, thermal buckling, elastic foundations, holes and cracks, local stiffness reductions, damage identification, local-global mode interaction, uncertainty quantification, and experimental verification.

For laminated plates, the isotropic bending rigidity has to be replaced by the laminate bending-stiffness matrix. Bending-twisting coupling and anisotropy can change both the critical load and the selected mode, which makes the present isotropic solution a useful baseline for more advanced composite models.

7. Conclusions

This paper is an educational case study in elastic stability and finite-element verification. Its main teaching messages are: (i) a finite-element eigenvalue result is credible only when the reference-load, sign, assembly, constraint, and sorting conventions are documented and checked against an independent solution; (ii) convergence must be quantified, not assumed, and slow convergence may come from the load introduction rather than the element; (iii) analytical minimization over the modal integers is needed to identify the governing plate mode; and (iv) a discrepancy between a shell-element result and thin-plate theory has to be split into discretization error and model-form (transverse-shear and support) error.

A reproducible analytical and finite-element buckling benchmark has been assembled for a pinned-pinned Euler-Bernoulli column and a simply supported rectangular plate. The 40-element beam model reproduces the first four Euler eigenvalues, and the observed order of convergence approaches four. For the plate, the Q4 flat-shell model and the ANSYS SHELL181 refinement both identify the governing pattern $(m, n) = (2, 1)$ and approach the Navier value, with first-mode errors of +0.0399% (Q4, 60×40 elements) and +0.547% (SHELL181, 48×32 elements). The slow SHELL181 convergence comes mainly from the equal nodal partition of the edge load, which overloads the corner nodes and produces a first-order error.

Both shell models converge to the shear-shifted Mindlin transition aspect ratios rather than to $\sqrt{m(m+1)}$. The shift is proportional to $(t/b)^2$ and amounts to -0.03% at $b/t = 100$ and -0.8% at $b/t = 20$ for the first transition, so the small error of the first crossing relative to $\sqrt{2}$ at $b/t = 100$ is partly a cancellation between a positive discretization error and a negative physical shift. Hard and soft simple support differ by 0.27% in the load at $b/t = 100$, a difference that has to be stated whenever shell results are compared with plate theory. For the column, the Timoshenko shear correction stays below 0.03% for $L/h \geq 100$ (Section 4.13), so the Euler-Bernoulli benchmark is adequate for the slender column studied.

The contribution is thus educational and methodological: the paper gives instructors and students a complete, transparent, and reusable worked example, and every number reported can be traced to the MATLAB, ANSYS, and Q4 files deposited in the supplementary package.

Data availability

The supplementary package is organized by purpose. The folder original_author_project contains the original MATLAB generator RUN_BUCKLING_STABILITY_STUDY.m, the ANSYS reproduction input decks, the project README, and the MAT/CSV/PNG/summary outputs supporting the baseline results. The folder flat_shell_validation contains the independent Q4 flat-shell source code,

mesh-convergence data, first-four-mode comparison, matrix-energy check, metadata, and figures; its mode_transition_localization subfolder contains the additional transition-localization script, CSV, figure, and run note. The folder ansys_shell181_validation contains the ANSYS production-resolution solver files and first-four mode data together with the executed structured mesh-convergence products. The folder audit contains the archive/source consistency report, checksum comparison, verification script, and the 40-element beam matrix-energy check. A provenance manifest and SHA-256 checksum list accompany the package. The folder mindlin_transition contains the MATLAB sources (Mindlin closed form, Q4 flat-shell solver, localization and post-processing scripts), the ANSYS APDL decks and result files of the transition scan and of the support and load-introduction test, the derived CSV tables, and the Python reference implementations used for cross-checking. The folder timoshenko_higher_order_verification contains the data of Table 11. The complete package is also deposited in a permanent public repository (Zenodo, https://doi.org/10.5281/zenodo.23170066, license CC BY 4.0).

References

[1] S. P. Timoshenko and J. M. Gere. *Theory of Elastic Stability*. McGraw-Hill, New York, 2nd edition, 1961.

[2] Z. P. Bažant and L. Cedolin. *Stability of Structures: Elastic, Inelastic, Fracture and Damage Theories*. Oxford University Press, New York, 1991.

[3] D. O. Brush and B. O. Almroth. *Buckling of Bars, Plates, and Shells*. McGraw-Hill, New York, 1975.

[4] J. M. T. Thompson and G. W. Hunt. *A General Theory of Elastic Stability*. Wiley, London, 1973.

[5] K. J. Bathe. *Finite Element Procedures*. Prentice Hall, Upper Saddle River, 1996.

[6] O. C. Zienkiewicz, R. L. Taylor, and J. Z. Zhu. *The Finite Element Method: Its Basis and Fundamentals*. Elsevier, Oxford, 7th edition, 2013.

[7] R. D. Cook, D. S. Malkus, M. E. Plesha, and R. J. Witt. *Concepts and Applications of Finite Element Analysis*. Wiley, New York, 4th edition, 2002.

[8] J. N. Reddy. *Theory and Analysis of Elastic Plates and Shells*. CRC Press, Boca Raton, 2nd edition, 2007.

[9] A. C. Ugural. *Stresses in Plates and Shells*. CRC Press, Boca Raton, 3rd edition, 2018.

[10] E. H. Mansfield. *The Bending and Stretching of Plates*. Cambridge University Press, Cambridge, 2nd edition, 1989.

[11] M. A. Patil and R. Kadoli. State-of-the-art in different formulations of super convergent mesh-less differential quadrature method. *Archives of Computational Methods in Engineering*, 33:4021–4058, 2026. Published online 18 October 2025. 10.1007/s11831-025-10423-4.

[12] W. Patel, M. A. Patil, A. Bodhe, S. Saraf, and R. Kadoli. On static and dynamic responses of smart magnetostrictive functionally graded plate: Modified fourier series and differential quadrature solution. *Thin-Walled Structures*, 218:113916, 2026. 10.1016/j.tws.2025.113916.

[13] F. Millar and D. Mora. A finite element method for the buckling problem of simply supported Kirchhoff plates. *Journal of Computational and Applied Mathematics*, 286:68–78, 2015. 10.1016/j.cam.2015.02.018.

[14] L.-W. He and C.-J. Cheng. A method of determining buckled states of thin plates at a double eigenvalue. *Applied Mathematics and Mechanics (English Edition)*, 13(4):325–329, 1992. 10.1007/BF02451418.

[15] C. M. Wang. Allowance for prebuckling deformations in buckling load relationship between Mindlin and Kirchhoff simply supported plates of general polygonal shape. *Engineering Structures*, 17(6):413–418, 1995. 10.1016/0141-0296(95)00042-6.

[16] C. M. Wang, S. Kitipornchai, and Y. Xiang. Relationships between buckling loads of Kirchhoff, Mindlin, and Reddy polygonal plates on Pasternak foundation. *Journal of Engineering Mechanics*, 123(11):1134–1137, 1997. 10.1061/(ASCE)0733-9399(1997)123:11(1134).

[17] C. M. Wang, J. N. Reddy, and K. H. Lee. *Shear Deformable Beams and Plates: Relationships with Classical Solutions*. Elsevier, Amsterdam, 2000.

[18] S. Hosseini-Hashemi, K. Khorshidi, and M. Amabili. Exact solution for linear buckling of rectangular Mindlin plates. *Journal of Sound and Vibration*, 315(1–2):318–342, 2008. 10.1016/j.jsv.2008.01.059.

[19] R. D. Mindlin. Influence of rotatory inertia and shear on flexural motions of isotropic, elastic plates. *Journal of Applied Mechanics*, 18:31–38, 1951. 10.1115/1.4010217.

[20] E. Reissner. The effect of transverse shear deformation on the bending of elastic plates. *Journal of Applied Mechanics*, 12:A69–A77, 1945. 10.1115/1.4009435.

[21] W. T. Koiter. *On the Stability of Elastic Equilibrium*. PhD thesis, Delft University of Technology, Delft, 1945.

[22] B. Budiansky. Theory of buckling and post-buckling behavior of elastic structures. *Advances in Applied Mechanics*, 14:1–65, 1974. 10.1016/S0065-2156(08)70030-9.

[23] M. Bohlooly Fotovat. Some unfamiliar structural stability aspects of unsymmetric laminated composite plates. *Materials*, 17(15):3856, 2024. 10.3390/ma17153856.

[24] K. J. Bathe and E. N. Dvorkin. A four-node plate bending element based on Mindlin/Reissner plate theory and a mixed interpolation. *International Journal for Numerical Methods in Engineering*, 21(2):367–383, 1985. 10.1002/nme.1620210213.

[25] E. J. Brunelle and S. R. Robertson. Initially stressed Mindlin plates. *AIAA Journal*, 12:1036–1045, 1974. 10.2514/3.49407.

[26] A. Belounar, F. Boussem, and A. Tati. A novel C0 strain-based finite element for free vibration and buckling analyses of functionally graded plates. *Journal of Vibration Engineering & Technologies*, 11:281–300, 2023. 10.1007/s42417-022-00577-x.